Main Manuscript for

Electronic Structure and Photophysics of a Supermolecular Iron Complex having a Long MLCT State Lifetime and Panchromatic Absorption

Ting Jiang,[1†] Yusong Bai,[1†] Peng Zhang,[1] Qiwei Han,[1] David B. Mitzi,[1,2] and Michael J. Therien[1*]

[1]Department of Chemistry, Duke University, Durham, North Carolina 27708-0346, USA.

[2]Department of Mechanical Engineering and Materials Science, Duke University, Durham, North Carolina 27708-0346, USA.

[†]These authors contributed equally to this work.

* Corresponding author: Michael Therien

Email: michael.therien@duke.edu

Classification

Physical Sciences: Chemistry

Keywords

Iron chromophore, metal-to-ligand charge transfer, excited-state dynamics

Author Contributions

M.J.T. conceived the project. T.J. designed, synthesized and characterized precursor and target molecular compositions. Y.B. performed the ultrafast pump-probe transient absorption and time-correlated single photon counting spectroscopic measurements, and analyzed these data. T.J. and Y.B. jointly carried out photoluminescence measurements. P.Z. performed computational studies. T.J., Y.B., and Q.H. jointly performed photocurrent−photovoltage measurements in DSSC device configurations. All authors discussed the results and contributed to writing manuscript.

Abstract

Exploiting earth-abundant iron-based metal complexes as high-performance photosensitizers demands long-lived electronically excited metal-to-ligand charge-transfer (MLCT) states, but these species suffer typically from femtosecond timescale CT-state quenching by low-lying nonreactive metal-centered (MC) states. Here, we engineer supermolecular Fe(II) chromophores based on the bis(tridentate-ligand)metal(II)-ethyne-(porphinato)zinc(II) conjugated framework, previously shown to give rise to highly delocalized low-lying ^{3}MLCT states for other Group VIII metal (Ru, Os) complexes. Electronic spectral, potentiometric, and ultrafast pump-probe transient dynamical data demonstrate that a combination of a strong σ-donating tridentate ligand and a (porphinato)zinc(II) moiety with low-lying π* energy levels, sufficiently destabilize MC states and stabilize supermolecular MLCT states to realize Fe(II) complexes that express ^{3}MLCT state photophysics reminiscent of their heavy metal analogues. The resulting Fe(II) chromophore archetype, FeNHCPZn, features a highly polarized charge transfer state having a profoundly extended ^{3}MLCT lifetime (160 ps), ^{3}MLCT phosphorescence, and ambient environment stability. Density functional and domain-based local pair natural orbital coupled cluster [DLPNO-CCSD(T)] theory reveal triplet state wavefunction spatial distributions consistent with electronic spectroscopic and excited-state dynamical data, further underscoring the dramatic Fe metal-to-extended ligand CT character of electronically excited FeNHCPZn. This design further prompts intense panchromatic absorptivity via redistributing high-energy absorptive oscillator strength throughout the visible spectral domain, while maintaining a substantial excited-state oxidation potential for wide-ranging photochemistry – highlighted by the ability of FeNHCPZn to photo-inject charges into a SnO_2/FTO electrode in a dye-sensitized solar cell (DSSC) architecture. Concepts enumerated herein afford new opportunities for replacing traditional rare-metal-based emitters for solar energy conversion and photo-luminescence applications.

Significance Statement

The main hurdle that prevents earth-abundant iron-based complexes from replacing environmentally unfriendly and expensive heavy metal (*e.g.*, Ru(II), Os(II), Ir(III)) complexes in solar energy conversion applications is the typical ultra-short (femtosecond timescale) charge-transfer state lifetime of Fe(II) chromophores. We provide a design roadmap to a new generation of efficient iron-based photosensitizers

and present a novel Fe(II) complex archetype, FeNHCPZn, which features a profoundly extended metal-to-ligand charge-transfer lifetime and a large transition dipole moment difference between its ground and [3]MLCT states. This novel supermolecular design promotes superior visible photon harvesting over classic metal complexes while assuring a triplet excited-state oxidation potential appropriate for charge injection into the conduction bands of common semiconductor electrode materials, highlighting its photosensitizing utility in DSSC architectures.

Introduction

Transition-metal-based photosensitizers are extensively exploited for solar energy conversion applications that include dye-sensitized solar cells (DSSCs) (1, 2), photoelectrochemical cells (3, 4), and photo-redox catalysis (5, 6), as well as in light-emitting diode technologies (7, 8). The long-lived metal-to-ligand charge-transfer (MLCT) states and moderate light absorptivity of ruthenium and iridium complexes make them the most widely utilized photosensitizers for these applications (9-11); however, their large-scale technological implementation is severely impeded by the rarity and toxicity of these metals. Replacing these metals with iron, the earth-abundant lighter congener of ruthenium, offers an attractive solution. Yet any energy conversion reaction that might be driven by iron complexes is challenging, as they typically suffer from femtosecond timescale quenching of their respective photo-reactive charge-transfer (CT) states by low-lying nonreactive metal-centered (MC) states (12-14). After decades of exploration, while novel Fe(III) complexes exhibiting up to nano-second timescale [2]LMCT (ligand-to-metal charge-transfer) lifetimes and [2]LMCT→[2]GS (ground state) fluorescence have been developed (15, 16), advancement of Fe(II) complexes that mimic the benchmark [3]MLCT state photophysics of their Ru(II)/Os(II) analogues, has long been overdue.

Fe(II)-based photosensitizer design strategies to promote extended [3]MLCT lifetimes (τ_{3MLCT}) through destabilizing MC states relative to MLCT states, have relied upon ligands that have been previously realized in analogous Ru(II) systems (13, 17-21). These Fe(II) coordination environments feature commonly strong-field (σ-donating, π-accepting) ligands that destabilize MC states, or ligands with low-energy π* orbitals that stabilize significantly MLCT states. However, unlike Ru(II) complexes, in which a wide range of ligand environments make possible [3]MLCT states having long nanosecond-to-microsecond

[3]MLCT lifetimes (22, 23), the significantly lower MC state energies of Fe(II) have long precluded the design of Fe(II) complexes that display analogous photophysical properties. For instance, McCusker has studied the effect of a near-perfect octahedral dcpp (2,6-bis(2-carboxypyridyl)pyridine)-based Fe(II) ligand environment, which facilitates stronger metal-ligand interaction relative to that afforded by the common tpy (2,2':6',2''-terpyridine) ligand, on MC state energies and excited state lifetimes (13). Although this strategy increases the ligand-field splitting to a point where the lowest energy ligand-field excited state becomes the [3]MC rather than the [5]MC state, an increase in the MLCT lifetime of $Fe(dcpp)_2^{2+}$ is not observed relative to that established for tris(2,2'-bipyridine)iron(II) ($[Fe(bpy)_3]^{2+}$). Other promising strategies to boost Fe(II) complex CT-state lifetimes have been introduced by Wärnmark and Gros that exploit strong σ-donating 2,6-bis(imidazol-2-ylidene)pyridine-derived N-heterocyclic carbene (NHC) ligands: air-stable Fe(II) complexes in such coordination environments demonstrate MLCT lifetimes up to an ~20 ps timescale (17-20, 24). Recent work is highlighted by an Fe(II) complex, $Fe(btz)_3^{2+}$ (btz = 3,3'-dimethyl-1,1'-bis(p-tolyl)-4,4'-bis(1,2,3-triazol-5-ylidene)), which features a 528 ps MLCT lifetime in an O_2-free environment (21). Nonetheless, practical applications of $Fe(btz)_3^{2+}$ are hindered by its instant oxidation to $Fe(btz)_3^{3+}$ once exposed to air, due to its low oxidation potential induced by the strong σ-donating NHC-based btz ligand. This observation signals that strategies that employ only strong σ-donating ligands to extend Fe(II) complex MLCT lifetimes have likely plateaued, and that further progress toward realizing rich MLCT photochemistry based on Fe(II) complexes requires entirely new molecular designs that realize simultaneously destabilized MC states and stabilized MLCT states.

We have demonstrated an exceptional and non-conventional approach to realize long-lived (> µs) globally-delocalized low-lying MLCT states in highly-conjugated Ru(II)/Os(II) metal complexes based on the bis(terpyridyl)metal(II)-ethyne-(porphinato)zinc(II) supermolecular framework (25-36), wherein the bis(terpyridyl)metal(II) (M = Ru(II)/Os(II)) and (porphinato)zinc(II) (PZn) units are connected via an ethyne unit that bridges the 4'-terpyridyl and porphyrin macrocycle *meso*-carbon positions, aligning the respective low energy transition moments of these chromophoric building blocks in a head-to-tail arrangement. The nature of this chromophore-to-chromophore connectivity effectively mixes PZn π-π* and metal polypyridyl-based charge-resonance absorption oscillator strength, giving rise to (i) high-oscillator-strength long-wavelength absorption manifolds, and (ii) low-lying, long-lived (µs timescale)

triplet states featuring highly polarized charge-separated (MLCT) character. For instance, in the Ru(II) archetype of this molecular framework (RuPZn, Chart 1), a significantly extended ^{3}MLCT lifetime of 43 μs is achieved that contrasts sharply the 250 ps ^{3}MLCT lifetime of the Ru(tpy)$_2$ benchmark (26, 27).

Here we exploit this molecular design concept in conjunction with the strong σ-donating NHC ligand to craft Fe(II) complexes that simultaneously realize extended ^{3}MLCT lifetimes and intensive visible-light absorptivity. Along this line, we synthesize two prototypical highly-conjugated Fe(II) complexes, FePZn and FeNHCPZn (Chart 1), Fe(II) analogues of RuPZn that also possess highly delocalized low-lying MLCT states and panchromatic absorptivity. We analyze the influence of excited-state interpigment electronic coupling and the nature of ligand electronic structure upon the ground-state absorptivity and excited-state relaxation dynamics in these highly-conjugated Fe(II) supermolecular complexes. Spectroscopic data show that (i) both FePZn and FeNHCPZn manifest a ten-fold increase in visible spectral domain transition oscillator strength relative to that of classic Fe(II) complexes, and (ii) while the ^{3}MLCT lifetime of FePZn differs little from that determined for [Fe(tpy)$_2$]$^{2+}$, FeNHCPZn exhibits nearly an order of magnitude amplification in ^{3}MLCT lifetime (τ = 160 ps) compared to the benchmark values of conventional air-stable Fe(II) complexes, and displays phosphorescence. Aided by such an extended ^{3}MLCT lifetime, panchromatic light absorptivity, and insights gleaned from state-of-the-art electronic structural studies, we demonstrate the utility of FeNHCPZn as a photosensitizer in a proof-of-principle DSSC architecture. This chromophore design concept outlined herein thus forms the basis for a new class of Fe(II) supermolecules with compelling ^{3}MLCT lifetimes, visible-light absorptivity, and gripping photophysical properties, suitable for replacing traditional Ru(II)-based photosensitizers in solar energy conversion applications.

Results and Discussion

Molecular Design and Electronic Absorption Spectroscopy. FePZn (Figure 1B) and FeNHCPZn (Figure 1C) manifest panchromatic absorption resulting from intense mixing of FeL$_2$ (L = tpy or NHC) MLCT and PZn B- and Q-excited states, in resemblance to the previously established RuPZn system (25-38) (Figure 1A); synthetic details and characterization data may be found in the Supporting Information. Both Fe(II) supermolecules feature an intense absorption band centered at ~440 nm with an extinction

coefficient exceeding 10^5 $M^{-1}cm^{-1}$; this manifold derives from mixing of the porphyrin (TIPS-E-PZn, structure shown in Figure 1) $^1\pi$-π^* B- (λ_{max} = 426 nm) and FeL_2 MLCT states. The prominent absorption band in the long-wavelength region (550 ~ 700 nm) of these FePZn and FeNHCPZn spectra (Figure 1B-C) exhibits substantial tpy-E-PZn or NHC-E-PZn $^1\pi$-π^* Q-band (550 ~ 650 nm) character; the enhanced absorptive oscillator strength of this manifold relative to those characteristic of simple porphyrin chromophores originates from symmetry breaking of the PZn in-plane electronic transitions and charge resonance interactions between the FeL_2 and PZn units that are made possible by the ethyne bridge. Apart from these transitions featuring substantial PZn-derived oscillator strength, note that the absorption band displaying significant MLCT character in the RuPZn (526 nm) spectrum (Figure 1A) is also prominent in the FePZn and FeNHCPZn absorption spectra, centered respectively at 567 and 516 nm. The redshifts of these MLCT transition band maxima of the Fe(II) supermolecules relative to those of the conventional FeL_2 benchmarks underscore the extent to which this state is stabilized by the π-expanded PZn-containing ligand motif. While we utilize "B", "Q", and "MLCT" labels for describing electronic absorption manifolds characteristic of RuPZn, FePZn, and FeNHCPZn, these descriptors only denote the dominant character of these transitions, as PZn B and Q, and metal complex MLCT electronic states mix extensively in these supermolecules (25-36); because the nature of conjugation in these chromophores aligns the ML_2 and PZn transition dipoles in a head-to-tail arrangement, extensive excited-state interpigment electronic communication is enforced that drives significant CT character in each of these lowest three singlet excited states. Integrated absorptive oscillator strengths of FePZn and FeNHCPZn over the 400 – 750 nm spectral range (Figure S8) are one order of magnitude higher than those of $Fe(tpy)_2$ and $Fe(NHC)_2$, emphasizing that FePZn and FeNHCPZn are much better visible light absorbers, especially with respect to the low-energy yellow and red spectral regions of the solar spectrum, which are commonly unabsorbed by conventional transition-metal sensitizers used in DSSCs.

Despite that FePZn and FeNHCPZn exhibit analogous electronic absorptive spectral signatures (Figure 1), note that the FeNHCPZn supermolecule highlights a substantial degree of MLCT transition stabilization relative to the FeNHC building block: the FeNHCPZn MLCT band (516 nm) is red-shifted 2500 cm^{-1} relative to that for $Fe(NHC)_2$ (457 nm); in contrast, the FePZn MLCT band (567 nm, overlapped with the PZn derived y-polarized Q band) redshifts only 480 cm^{-1} with respect to the $Fe(tpy)_2$ MLCT band

(552 nm). This picture is congruent with the relative LUMO energy levels of tpy, NHC, and PZn as probed by potentiometric and computational methods (*vide infra*).

Potentiometric Properties. Oxidative and reductive electrochemical data indicate that for Ru-PZn (25), FePZn, and FeNHCPZn, the observed anodic and cathodic potentiometric responses trace their genesis to established bis(ligand)metal (Ru/FeL$_2$)- and PZn-redox processes, indicating that the singly and doubly oxidized- and reduced-ground states of these species correspond to cation and anion states that are localized predominantly on the building block chromophores of these supermolecules (Figure 2; Figure S7). These potentiometric data provide insight into MLCT and MC states energy levels, and the nature of electronic transition polarization in these supermolecules. Note in this regard that: (i) the $E(\text{Fe}^{2+/3+})$ values of both Fe(II) supermolecules are almost identical to their FeL$_2$ benchmarks, indicating that the σ-donating/π-accepting properties of the tpy/NHC ligand motifs (and thus the MC state energy levels) are unperturbed despite being linked to a highly-conjugated PZn π-framework, and (ii) FeNHCPZn manifests PZn$^{-/0}$-based reduction potential ($E_{1/2}^{-/0}$ = −1.15 V) at significantly higher potential than the $E_{1/2}^{-/0}$ value for Fe(NHC)$_2$ (-1.96 V) (17), contrasting the nature of the E$^{-/0}$ and E$^{2-/-}$ redox processes for FePZn (Figure 2). With respect to this latter point, note that the E$^{2-/-}$ redox process for FeNHCPZn that would localize substantial electron density on the Fe(NHC)$_2$ fragment, lies outside the solvent window afforded by acetonitrile solvent. These potentiometric data are thus congruent with a picture that emphasizes that while the MLCT state of FePZn will feature electron density polarized toward the tpy moiety, the corresponding MLCT state of FeNHCPZn will have a much greater transition moment, with electron density delocalized substantially on the conjugated PZn macrocycle (*vide infra*). The similarity of FeNHCPZn potentiometric (ΔE_p = [$E_{1/2}(\text{Fe}^{2+/3+})$ − $E_{1/2}(\text{L}^{0/-})$]) and optical (ΔE_{op}) bandgaps underscores this point. ΔE_p for FeNHCPZn (1.91 eV) is diminished 0.79 V relative to that for Fe(NHC)$_2$ (2.70 eV), much larger than the corresponding 0.21 eV drop in the magnitude of ΔE_p manifested for FePZn relative to Fe(Tpy)$_2$. ΔE_p(FeNHCPZn) matches the energy of its lowest energy optical transition energy (ΔE_{op} = 642 nm; 1.93 eV) emphasizing that electronic excitation gives rise to low-lying excited state having substantial CT character.

Excited-State Dynamics. Ultrafast pump-probe transient absorption spectroscopic data acquired at early delay times (< 1 ps) demonstrate that both FePZn and FeNHCPZn exhibit excited state absorption

features similar to those characteristic of bis(terpyridyl)metal(II)-ethyne-(porphinato)zinc supermolecules such as RuPZn (Figure 3) (26-36). Immediately following $S_0 \rightarrow S_1$ photoexcitation, NIR transient absorption signals centered at ~780 nm are evident for both Fe(II) supermolecules (Figure 3 B-C). This low-energy NIR signal, absent in the early delay time transient absorption spectra of the NHC-ethyne-PZn ligand alone (Figure S10), is characteristic of the $S_1 \rightarrow S_n$ absorptive manifold of the bis(terpyridyl)metal-ethyne-(porphinato)zinc supermolecules (see that of RuPZn in Figure 3A) (26-36). The decay of this $S_1 \rightarrow S_n$ absorptive manifold correlates with the rise of a new NIR transient absorptive signal centered at ~970 nm for FePZn and ~930 nm for FeNHCPZn, indicating the evolution of a new electronically excited state. This time-dependent transient spectral evolution is akin to that evinced for RuPZn, wherein this lower-energy NIR transient absorption signal has been shown to be a signature of an extensively delocalized low-lying triplet state having substantial MLCT character (26-36). In this regard, note that the FeNHCPZn NIR transient absorptive manifold centered at ~930 nm evinces positive solvatochromism with decreasing solvent polarity (Figure S11), corroborating the CT character of this excited state. For these reasons, coupled with substantial literature precedent (26-36), we denote the transient absorption manifold centered in this low energy NIR spectral region (~970 nm for FePZn and ~930 nm for FeNHCPZn) as a $T_{MLCT} \rightarrow T_n$ transition, and a spectroscopic hallmark of the MLCT state in these supermolecules; the rise time of this $T_{MLCT} \rightarrow T_n$ signal thus corresponds to $S_1 \rightarrow {}^3MLCT$ intersystem crossing dynamics (τ_{ISC} ~0.1 ps for FePZn and τ_{ISC} = 0.3 ps for FeNHCPZn).

However, at longer delay times (t > 1 ps), while the excited state absorption features of FePZn resemble those of conventional Fe(II) complexes such as $Fe(tpy)_2$ (17), FeNHCPZn spectral evolution shows remarkable correspondence to that manifest by the RuPZn benchmark, congruent with the fact that this ligand design realizes an Fe(II) complex that features a low-lying excited state that recapitulates the MLCT photophysics elucidated for (polypyridyl)metal(II)-ethyne-(porphinato)zinc(II) supermolecular chromophores that exploit the heavy metals ruthenium and osmium (26-36). In sharp contrast to FeNHCPZn, the FePZn ${}^3MLCT$ state decays on an ultrafast timescale, accompanied by the rise of a new transient absorption signal having substantial oscillator strength over the ~450-500 nm spectral region, which lies to the red of the PZn-derived B band bleaching signal. Given that (i) this nascent transient absorption signal decays in a few nanoseconds, close to that for ${}^5MC$ state lifetimes typical for $Fe(tpy)_2$

derivatives (17), and (ii) the transient signature associated with $^5MC\rightarrow{}^nMC^*$ absorption (where $^nMC^*$ denotes a higher lying, metal-centered electronically excited state) commonly lies to the red of the ligand-derived ground-state absorption bleaching signals (39, 40), we assign this transient absorption signal at ~450-500 nm as a FePZn $^5MC\rightarrow{}^nMC^*$ transition. The transient absorptive signatures characteristic of the S_1, ^3MLCT, and ^5MC states, and their corresponding time-dependent spectral evolution, indicate that $^3MLCT\rightarrow{}^5MC$ conversion dominates FePZn ^3MLCT state relaxation dynamics, and signifies that the ^3MLCT state of FePZn lies higher in energy than these MC states. Note that FeNHCPZn relaxation dynamics stand in marked juxtaposition to those described for FePZn, as FeNHCPZn's ^3MLCT NIR absorption decays simultaneously with the ground state recovery (τ_{3MLCT} = 160 ps; Figure 3C; Figure 4), without the observance of any other new excited state absorption signals: this excited-state dynamical behavior is identical to that manifest by RuPZn (26-36). These data thus indicate that $^{3,5}MC$ states play a negligible role in excited-state relaxation processes associated with the ^3MLCT state of FeNHCPZn. The Figure 4A Jablonski diagram summarizes the relative energetic arrangements of these FePZn and FeNHCPZn electronic states and their corresponding excited-state relaxation dynamics elucidated by pump-probe transient absorption spectroscopy and time-resolved emission experiments (*vide infra*).

Electronic Structural Studies. DFT calculations (41) that reveal frontier orbital energy levels, the nature of singly occupied molecular orbitals (SOMOs) that describe electronically excited triplet and quintet states, the spatial distribution of excited-state wavefunctions, and the magnitudes of FePZn and FeNHCPZn ground- and excited-state dipole moments, corroborate conclusions derived from electronic spectral, potentiometric, and time-resolved transient dynamical data. These comprehensive DFT computational studies exploit three different DFT functionals (M06L, B3LYP, and TPSSh); results stemming from these computations were further verified using domain-based local pair natural orbital coupled cluster (DLPNO-CCSD(T)) theory. These latter computational studies are particularly significant as DLPNO-CCSD(T) theory is designed to reproduce ~99.9% of the canonical correlation energy, and defines the present quantum mechanical "gold-standard" for determining molecular state energies (computational details are provided in the Supporting Information) (42, 43). Table 1 displays the ground-state singlet, and electronically excited triplet (T_1) and quintet (Q_1) state energetic minima (eV), computed using DFT and DLPNO-CCSD(T) theory for FePZn and FeNHCPZn. Note that for FePZn, the calculated

lowest Q_1 state energy is lower than its T_1 state energy, mirroring the ultrafast pump-probe transient dynamical results (Figure 3); in contrast, for FeNHCPZn, this picture is reversed – the calculated FeNHCPZn T_1 state resides much lower energy than its Q_1 state. The SOMOs that describe the FeNHCPZn T_1 state are shown in Figure 5; note that $SOMO_A$ shows electron density localized primarily at the Fe metal center, while $SOMO_B$ depicts electron density delocalized over the extended NHC-ethyne-PZn ligand framework, with the lion's share of electron density concentrated on the porphyrin macrocycle. These Figure 5 SOMOs highlight the intense MLCT character of the FeNHCPZn T_1 state. Table 2 highlights computational data that characterize the dipole moment magnitudes of the ground and lowest energy triplet and quintet states for FePZn and FeNHCPZn. While the lowest energy T_1 and Q_1 states of FePZn reflect dipole moments that resemble its S_0 state, the FeNHCPZn lowest energy T_1 and Q_1 states manifest dipole moments 30 Debye greater than that of its ground state. These computational analyses (Supporting Information) thus reinforce the Figure 4 Jablonski diagram derived from experiment, and emphasize the diminished roles played by MC states in FeNHCPZn excited-state relaxation dynamics. As FeNHCPZn T_1 state electron density is extensively polarized towards the PZn unit of the ligand framework, this ^{3}MLCT state concomitantly minimizes ^{3}MLCT–^{3,5}MC and ^{3}MLCT−S_0 wavefunction overlap relative to that characteristic of many benchmark photosensitizers, driving the long ^{3}MLCT state lifetime of FeNHCPZn.

Owing to the substantially extended FeNHCPZn ^{3}MLCT lifetime relative to that of FePZn and other conventional Fe(II) complexes, supermolecular ^{3}MLCT→S_0 phosphorescence from FeNHCPZn is observed. Photoexcitation of FeNHCPZn in a 1:1 MeCN:H_2O solvent mixture gives rise to weak room-temperature photoluminescence centered at 880 nm (Figure 4C). Time-correlated single photon counting determines a photoluminescence lifetime of 175 ps (Figure 4D), in close agreement with the 160 ps ^{3}MLCT lifetime acquired from ultrafast pump-probe spectroscopic data. The magnitudes of these matched lifetimes, coupled with the energy separation between the absorption and emission band maxima (Stokes shift = 3076 cm^{-1}) are consistent with assignment of the FeNHCPZn photoluminescence as phosphorescence resulting from a ^{3}MLCT→S_0 radiative transition (44); note that the magnitude of this Stokes shift resembles that evinced for RuPZn phosphorescence (35). Despite the weak nature of this room temperature phosphorescence, these data (i) provide an important measure of the ^{3}MLCT state

energy ($E_{0,0}$ = 810 nm = 1.53 eV) and (ii) demonstrate direct ^{3}MLCT→S_0 photoluminescence from an Fe(II) complex using a conventional excitation source that does not employ fluorescence upconversion experimental methods (45, 46). Moreover, these transient absorptive and emission experiments establish that FeNHCPZn is extraordinarily robust, as no evidence of photobleaching is observed in any of these ambient temperature photophysical experiments.

Beyond these excited-state dynamical and electronic structural properties, the promising utility of FeNHCPZn is also highlighted by the relative energetic arrangement between its triplet excited-state oxidation potential ($^3E^{*/+}$) and the conduction bands (CBs) of widely exploited semiconductor electrode materials (Figure S12A). The FeNHCPZn $^3E^{*/+}$ value (−0.77 V, *vs.* SCE, Figure S12A; Eq. S1) indicates exergonic driving forces for electron injection into the CBs of TiO_2 (−0.74 V, *vs.* SCE) and SnO_2 (−0.24 V, *vs.* SCE), two n-type semiconductor electrode materials commonly used in DSSCs (4). Figure S12B-C data highlight the efficacy of FeNHCPZn as a DSSC photosensitizer in a regenerative cell architecture that exploits a FeNHCPZn-sensitized photoelectrode (FeNHCPZn/SnO_2/FTO); further details are provided in the Supporting Information. Pump-probe transient absorption spectroscopic experiments that interrogate FeNHCPZn-anchored SnO_2 particles corroborate that electron injection into the semiconductor derives from a FeNHCPZn excited state produced via visible light absorption (Figure S13). We emphasize that the measured J_{SC} and V_{OC} responses in this regenerative cell represent a rare, if not unique example, of a substantial photosensitization effect achieved in a device architecture using an Fe(II) MLCT chromophore (47-50).

Conclusion

In this work, we define a robust air-stable Fe(II) complex, FeNHCPZn, that features both a sub-nanosecond ^{3}MLCT lifetime and intensive visible-light absorption by applying a non-conventional chromophore engineering strategy based on the bis(tridentate-ligand)metal(II)-ethyne-(porphinato)zinc(II) conjugated framework. This molecular framework, decouples ligand functions that destabilize MC states from those that lead to stabilized MLCT states in the FeNHCPZn supermolecule. Electronic spectral, potentiometric, and ultrafast time-resolved pump-probe transient dynamical data emphasize that electronic excitation of FeNHCPZn gives rise to a low-lying ^{3}MLCT excited state having substantial

charge-transfer character; state-of-the-art electronic structural computations, using domain-based local pair natural orbital coupled cluster (DLPNO-CCSD(T)) theory, demonstrate the unusual nature of the FeNHCPZn electronically excited triplet (T_1) state: in contrast to conventional Fe(II) complexes, it lies substantially lower in energy than its corresponding quintet (Q_1) state and features a dipole moment amplified by 30 Debye relative its ground state. The long 160 ps FeNHCPZn ^{3}MLCT state lifetime at ambient temperature, coupled with its substantial $^3E^{*/+}$ potential, high oscillator strength UV-vis panchromatic absorptive properties, and ability to serve as a photosensitizer in a DSSC architecture, demonstrate new possibilities for exploiting Fe(II) complexes in solar energy conversion applications, as photoluminescent materials, and as photo-redox catalysts. Chromophore designs that further augment the extent of MLCT state polarization and stabilization in FeNHC-expanded conjugated ligand frameworks (e.g., by modulating PZn motif π^* energy levels via electron-withdrawing groups, or replacing PZn with other π- polarizable units) offer opportunities to push Fe(II) complex MLCT lifetimes to the sub-µs timescale. We anticipate that this new class of earth-abundant Fe-based photosensitizers with long MLCT excited-state lifetimes and intense visible-light absorption will serve to advance opportunities for environment-friendly and low-cost solar energy conversion.

Materials and Methods

Synthetic Materials. Tetrahydrofuran (THF) was purchased from Sigma-Aldrich (Inhibitor free, HPLC grade) and distilled over sodium and benzophenone before use. Diisopropylamine was purchased from Sigma-Aldrich (redistilled, 99.95%). All other solvents utilized in syntheses were purchased from Fisher Scientific (HPLC grade). Acetonitrile was dried over calcium hydride and distilled. All other reagents were used as received (Aldrich or Fisher). Chromatographic purification (silica gel 60, 230-400 mesh, EM Science; aluminum oxide, 50-200 µm, 60 Å, Acros Organics; Bio-Beads S-X1, 200-400 mesh, BioRad) of all newly synthesized compounds was accomplished on the bench top.

General Characterization Instruments. A 400 MHz Brüker spectrometer was used to obtain NMR spectra for all synthesized compounds. Chemical shifts for 1H NMR spectra are reported relative to residual protium in deuterated solvents (δ (residual) = 7.26 ppm in CDCl3, δ (residual) = 1.94 ppm in CD3CN, δ (residual) = 2.05 ppm in acetone-d6, δ (residual) = 1.72 ppm in THF-d8). All J values are

reported in Hertz. Reported MALDI-TOF data were acquired with an Applied Biosystems DE-Pro MALDI-MS at the Department of Chemistry at Duke University. Samples were prepared as micromolar solutions in acetone, using HABA (2-(4-hydroxyphenylazo)benzoic acid) as the matrix. Electronic absorption spectra were acquired on a Shimadzu Pharmaspec UV-1700 spectrometer.

Acknowledgements

References

1. B. O'Regan, M. Grätzel, A low-cost, high-efficiency solar cell based on dye-sensitized colloidal TiO_2 films. *Nature* **353**, 737-740 (1991).
2. A. Hagfeldt, G. Boschloo, L. C. Sun, L. Kloo, H. Pettersson, Dye-sensitized solar cells. *Chem. Rev.* **110**, 6595-6663 (2010).
3. W. J. Youngblood *et al.*, Photoassisted overall water splitting in a visible light-absorbing dye-sensitized photoelectrochemical cell. *J. Am. Chem. Soc.* **131**, 926-927 (2009).
4. D. L. Ashford *et al.*, Molecular chromophore-catalyst assemblies for solar fuel applications. *Chem. Rev.* **115**, 13006-13049 (2015).
5. C. K. Prier, D. A. Rankic, D. W. C. MacMillan, Visible light photoredox catalysis with transition metal complexes: applications in organic synthesis. *Chem. Rev.* **113**, 5322-5363 (2013).
6. D. M. Schultz, T. P. Yoon, Solar synthesis: Prospects in visible light photocatalysis. *Science* **343**, 1239176 (2014).
7. M. J. Jurow *et al.*, Understanding and predicting the orientation of heteroleptic phosphors in organic light-emitting materials. *Nat. Mater.* **15**, 85-91 (2016).
8. J. Lee *et al.*, Deep blue phosphorescent organic light-emitting diodes with very high brightness and efficiency. *Nat. Mater.* **15**, 92-98 (2016).
9. L. Flamigni, J.-P. Collin, J.-P. Sauvage, Iridium terpyridine complexes as functional assembling units in arrays for the conversion of light energy. *Acc. Chem. Res.* **41**, 857-871 (2008).
10. G. C. Vougioukalakis, A. I. Philippopoulos, T. Stergiopoulos, P. Falaras, Contributions to the development of ruthenium-based sensitizers for dye-sensitized solar cells. *Coord. Chem. Rev.* **255**, 2602-2621 (2011).
11. H. Xu *et al.*, Recent progress in metal-organic complexes for optoelectronic applications. *Chem. Soc. Rev.* **43**, 3259-3302 (2014).
12. J. E. Monat, J. K. McCusker, Femtosecond excited-state dynamics of an Iron(II) polypyridyl solar cell sensitizer model. *J. Am. Chem. Soc.* **122**, 4092-4097 (2000).
13. L. L. Jamula, A. M. Brown, D. Guo, J. K. McCusker, Synthesis and characterization of a high-symmetry ferrous polypyridyl complex: approaching the $^5T_2/^3T_1$ crossing point for Fe^{II}. *Inorg. Chem.* **53**, 15-17 (2014).
14. A. K. C. Mengel *et al.*, A heteroleptic push–pull substituted iron(II) bis(tridentate) complex with low-energy charge-transfer states. *Chem. Eur. J.* **21**, 704-714 (2015).
15. P. Chábera *et al.*, A low-spin Fe(III) complex with 100-ps ligand-to-metal charge transfer photoluminescence. *Nature* **543**, 695-699 (2017).

16.   K. S. Kjær *et al.*, Luminescence and reactivity of a charge-transfer excited iron complex with nanosecond lifetime. *Science* **363**, 249-253 (2019).

17.   Y. Liu *et al.*, Towards longer-lived metal-to-ligand charge transfer states of iron(II) complexes: an N-heterocyclic carbene approach. *Chem. Commun.* **49**, 6412-6414 (2013).

18.   Y. Liu *et al.*, A heteroleptic ferrous complex with mesoionic bis(1,2,3-triazol-5-ylidene) ligands: taming the MLCT excited state of iron(II). *Chem. Eur. J.* **21**, 3628-3639 (2015).

19.   L. Liu *et al.*, A new record excited state [3]MLCT lifetime for metalorganic iron(II) complexes. *Phys. Chem. Chem. Phys.* **18**, 12550-12556 (2016).

20.   Y. Liu, P. Persson, V. Sundström, K. Wärnmark, Fe N-heterocyclic carbene complexes as promising photosensitizers. *Acc. Chem. Res.* **49**, 1477-1485 (2016).

21.   P. Chábera *et al.*, Fe(II) Hexa N-heterocyclic carbene complex with a 528 ps metal-to-ligand charge-transfer excited-state lifetime. *J Phys Chem Lett* **9**, 459-463 (2018).

22.   M. Abrahamsson *et al.*, Bistridentate ruthenium(II)polypyridyl-type complexes with microsecond [3]MLCT state lifetimes: Sensitizers for rod-like molecular arrays. *J. Am. Chem. Soc.* **130**, 15533-15542 (2008).

23.   A. K. Pal, G. S. Hanan, Design, synthesis and excited-state properties of mononuclear Ru(II) complexes of tridentate heterocyclic ligands. *Chem. Soc. Rev.* **43**, 6184-6197 (2014).

24.   P. Zimmer *et al.*, The connection between NHC ligand count and photophysical properties in Fe(II) photosensitizers: An experimental study. *Inorg. Chem.* **57**, 360-373 (2018).

25.   H. T. Uyeda *et al.*, Unusual frequency dispersion effects of the nonlinear optical response in highly conjugated (polypyridyl)metal−(porphinato)zinc(II) chromophores. *J. Am. Chem. Soc.* **124**, 13806-13813 (2002).

26.   T. V. Duncan, I. V. Rubtsov, H. T. Uyeda, M. J. Therien, Highly conjugated (polypyridyl)metal-(porphinato)zinc(II) compounds: Long-lived, high oscillator strength, excited-state absorbers having exceptional spectral coverage of the near-infrared. *J. Am. Chem. Soc.* **126**, 9474-9475 (2004).

27.   T. V. Duncan, T. Ishizuka, M. J. Therien, Molecular engineering of intensely near-infrared absorbing excited states in highly conjugated oligo(porphinato)zinc-(polypyridyl)metal(II) supermolecules. *J. Am. Chem. Soc.* **129**, 9691-9703 (2007).

28.   T. N. Singh-Rachford *et al.*, Supermolecular-chromophore-sensitized near-infrared-to-visible photon upconversion. *J. Am. Chem. Soc.* **132**, 14203-14211 (2010).

29.   T. Ishizuka *et al.*, The roles of molecular structure and effective optical symmetry in evolving dipolar chromophoric building blocks to potent octopolar nonlinear optical chromophores. *J. Am. Chem. Soc.* **133**, 2884-2896 (2011).

30.   H. C. Fry *et al.*, Computational de novo design and characterization of a protein that selectively binds a highly hyperpolarizable abiological chromophore. *J. Am. Chem. Soc.* **135**, 13914-13926 (2013).

31.   J.-H. Olivier *et al.*, Near-infrared-to-visible photon upconversion enabled by conjugated porphyrinic sensitizers under low-power noncoherent illumination. *J. Phys. Chem. A* **119**, 5642-5649 (2015).

32.   A. Nayak *et al.*, Large hyperpolarizabilities at telecommunication-relevant wavelengths in donor–acceptor–donor nonlinear optical chromophores. *ACS Cent. Sci.* **2**, 954-966 (2016).

33.   T. Jiang, N. F. Polizzi, J. Rawson, M. J. Therien, Engineering high-potential photo-oxidants with panchromatic absorption. *J. Am. Chem. Soc.* **139**, 8412-8415 (2017).

34.   Y. Bai *et al.*, Molecular road map to tuning ground state absorption and excited state dynamics of long-wavelength absorbers. *J. Am. Chem. Soc.* **139**, 16946-16958 (2017).

35.   N. F. Polizzi, T. Jiang, D. N. Beratan, M. J. Therien, Engineering opposite electronic polarization of singlet and triplet states increases the yield of high-energy photoproducts. *Proc. Natl. Acad. Sci. U.S.A.* **116**, 14465 (2019).

36.   B. Shan *et al.*, Excitation energy-dependent photocurrent switching in a single-molecule photodiode. *Proc. Natl. Acad. Sci. U.S.A.* **116**, 16198 (2019).

37.   S. Keinan, M. J. Therien, D. N. Beratan, W. Yang, Molecular design of porphyrin-based nonlinear optical materials. *J. Phys. Chem. A* **112**, 12203-12207 (2008).

38.   X. Hu *et al.*, Predicting the frequency dispersion of electronic hyperpolarizabilities on the basis of absorption data and Thomas−Kuhn sum rules. *J. Phys. Chem. C* **114**, 2349-2359 (2010).

39.   A. L. Smeigh, M. Creelman, R. A. Mathies, J. K. McCusker, Femtosecond time-resolved optical and Raman spectroscopy of photoinduced spin crossover: Temporal resolution of low-to-high spin optical switching. *J. Am. Chem. Soc.* **130**, 14105 (2008).

40.   G. Auböck, M. Chergui, Sub-50-fs photoinduced spin crossover in $[Fe(bpy)_3]^{2+}$. *Nat. Chem.* **7**, 629-633 (2015).

41.   M. J. Frisch *et al.* (2016) Gaussian 16 Rev. C.01. (Wallingford, CT, Gaussian 16).

42.   Y. Guo, Riplinger, C., Becker, U., Liakos, D. G., Minenkov, Y., Cavallo, L., Neese, F., An improved linear scaling perturbative triples correction for the domain based local pair-natural orbital based singles and doubles coupled cluster method [DLPNO-CCSD (T)]. *J. Chem. Phys.* **148**, 011101 (2018).

43.   F. N. Masaaki Saitow, Accurate spin-densities based on the domain-based local pair-natural orbital coupled-cluster theory. *J. Chem. Phys.* **149**, 034104 (2018).

44.   Given the weak nature of this emission, laser excitation was utilized.

45.   W. Gawelda *et al.*, Ultrafast nonadiabatic dynamics of $[Fe^{II}(bpy)_3]^{2+}$ in solution. *J. Am. Chem. Soc.* **129**, 8199-8206 (2007).

46.   J. Šima (2015) (Non)luminescent properties of iron compounds. *Acta Chim. Slov.* **8**, 126-132 (2015).

47.   While no attempt was made to optimize device performance, we note that an identical cell that featured a chromophore/SnO_2/FTO photoanode and exploited the benchmark N3 dye gave rise to JSC = 2.1 mA/cm^2 and VOC = 0.32 V, when examined under identical conditions (Fig. S10).

48.   M. K. Nazeeruddin *et al.*, Conversion of light to electricity by cis-X_2bis(2,2'-bipyridyl-4,4'-dicarboxylate)ruthenium(II) charge-transfer sensitizers (X = Cl-, Br-, I-, CN-, and SCN-) on nanocrystalline titanium dioxide electrodes. *J. Am. Chem. Soc.* **115**, 6382-6390 (1993).

49.   S. Ferrere, B. A. Gregg, Photosensitization of TiO_2 by $[Fe^{II}(2,2'$-bipyridine-4,4'-dicarboxylic acid)$_2(CN)_2]$: Band selective electron injection from ultra-short-lived excited states. *J. Am. Chem. Soc.* **120**, 843-844 (1998).

50.   T. Duchanois *et al.*, An iron-based photosensitizer with extended excited-state lifetime: Photophysical and photovoltaic properties. *Eur. J. Inorg. Chem.* **14**, 2469-2477 (2015).

Figures and Tables

Chart 1. Design flow of supermolecular Fe(II) complexes (FePZn, FeNHCPZn) that realize sub-nanosecond ^{3}MLCT lifetimes and intensive visible-light absorption based on the RuPZn archetype and the bis(tridentate-ligand)metal(II)-(porphinato)zinc(II) framework.
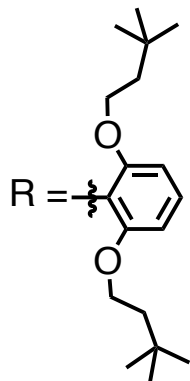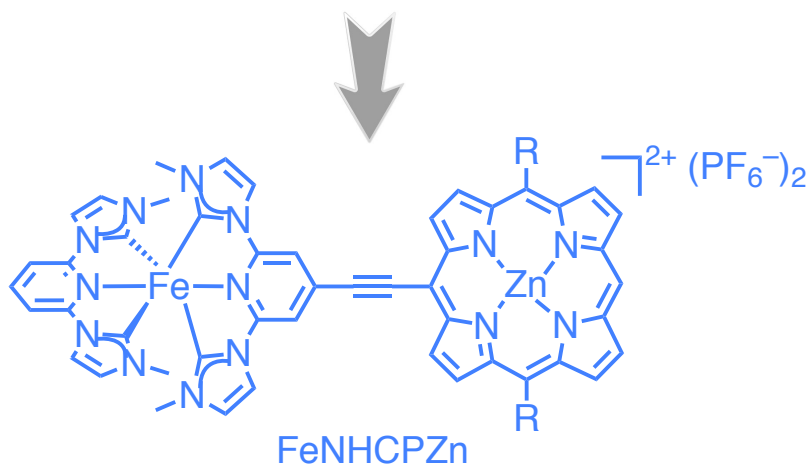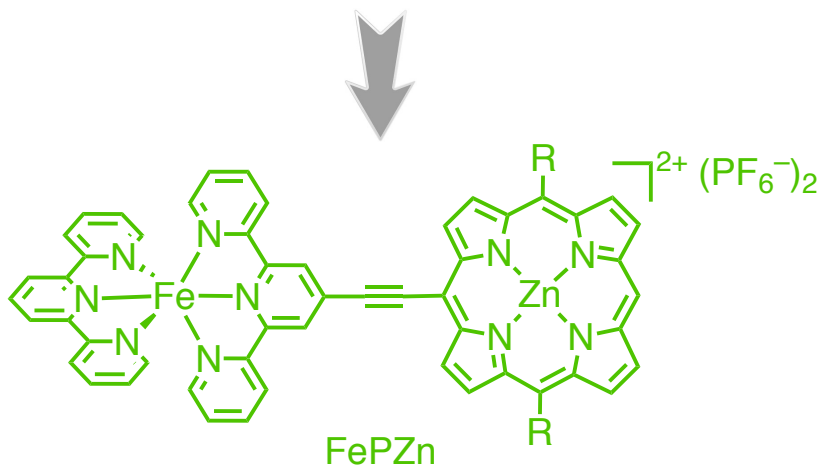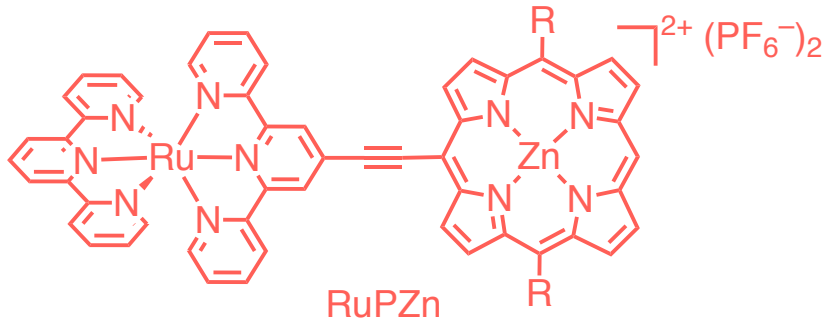

Figure 1. Electronic absorption spectra of RuPZn (**A**), FePZn (**B**), and FeNHCPZn (**C**), together with those of the Ru(tpy)$_2$, Fe(tpy)$_2$, Fe(NHC)$_2$, tpy-E-PZn and NHC-E-PZn building blocks, over the 250–750 nm wavelength range; spectra of all compounds were recorded in acetonitrile solvent, save NHC-E-PZn, which was recorded in methylene chloride. Note that the ordinates in these figure panels reflect the extinction coefficients of RuPZn FePZn, FeNHCPZn, Ru(tpy)$_2$, Fe(tpy)$_2$, and Fe(NHC)$_2$; tpy-E-PZn spectra are shown scaled respectively to the RuPZn and FePZn spectra of panels A and B, and the NHC-E-PZn spectrum is shown scaled to that for FeNHCPZn in panel C, for comparative purposes.
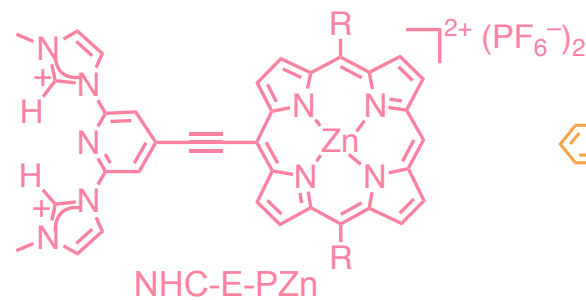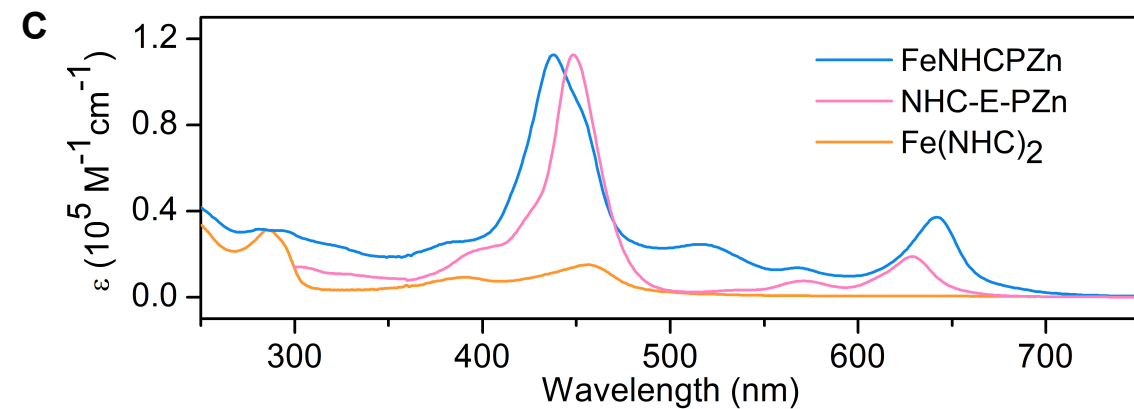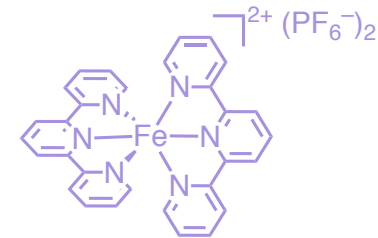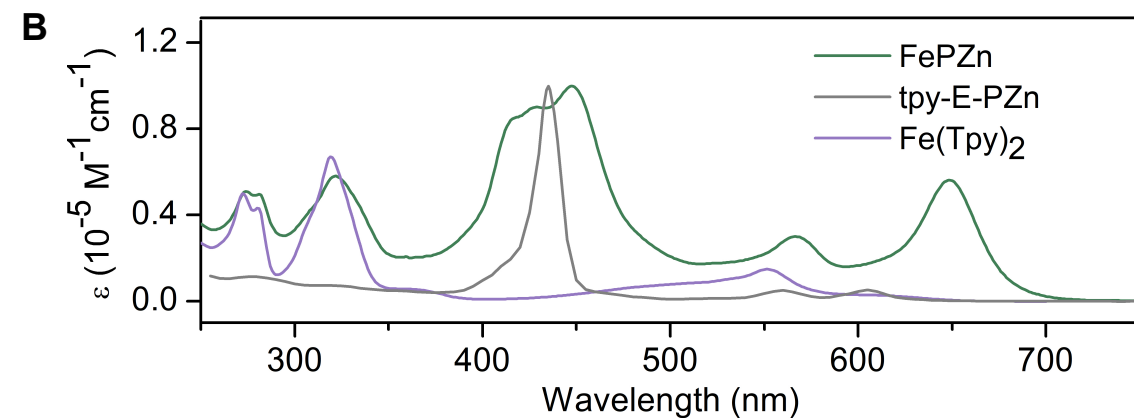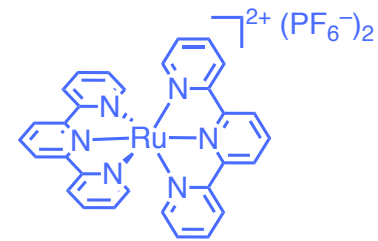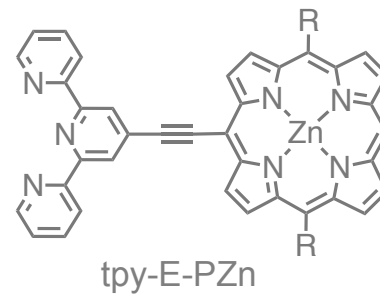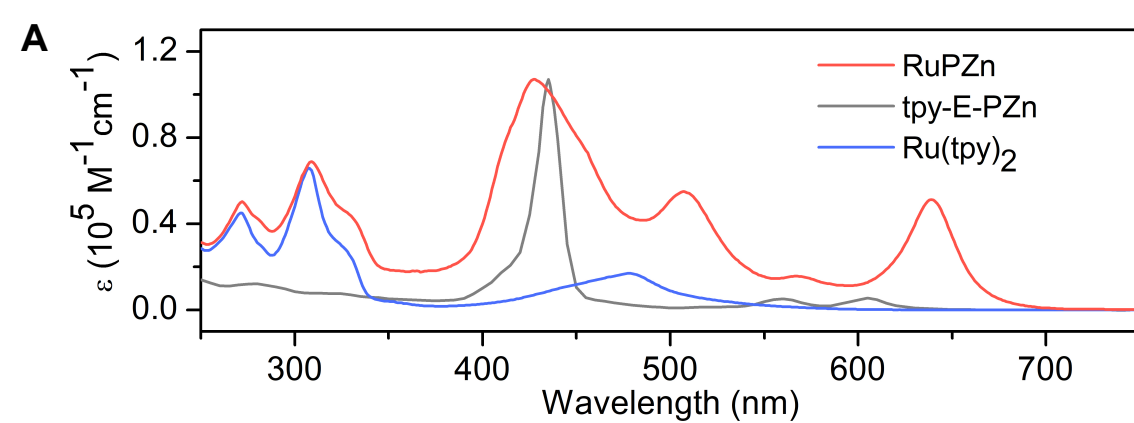
Figure 2. Redox potentials (vs. SCE) of RuPZn, FePZn, and FeNHCPZn, together with those of the Ru(tpy)$_2$, Fe(tpy)$_2$, Fe(NHC)$_2$ and TIPS-E-PZn building blocks. $E^{x/y}$ denotes the overall redox state of the corresponding supramolecular structure, while information followed in parentheses highlights the key structural motif being oxidized/reduced. Experimental conditions: 0.1 M [(n-C$_4$H$_9$)$_4$N][PF$_6$], T = 20 °C; RuPZn, FePZn, FeNHCPZn, Ru(tpy)$_2$, Fe(tpy)$_2$, and Fe(NHC)$_2$ - CH$_3$CN solvent, TIPS-E-PZn - CH$_2$Cl$_2$ solvent.

Figure 3. Representative ultrafast pump-probe spectra recorded at several time delays, and exemplary kinetic traces at key probe wavelengths for RuPZn (**A, D**), FePZn (**B, E**), and FeNHCPZn (**C, F**). Experimental conditions: solvent = MeCN; temperature = 21 °C; magic angle polarization; λ_{ex} = 650 nm for RuPZn and FeNHCPZn, λ_{ex} = 670 nm for FePZn; P_{ex} = 300 µW.
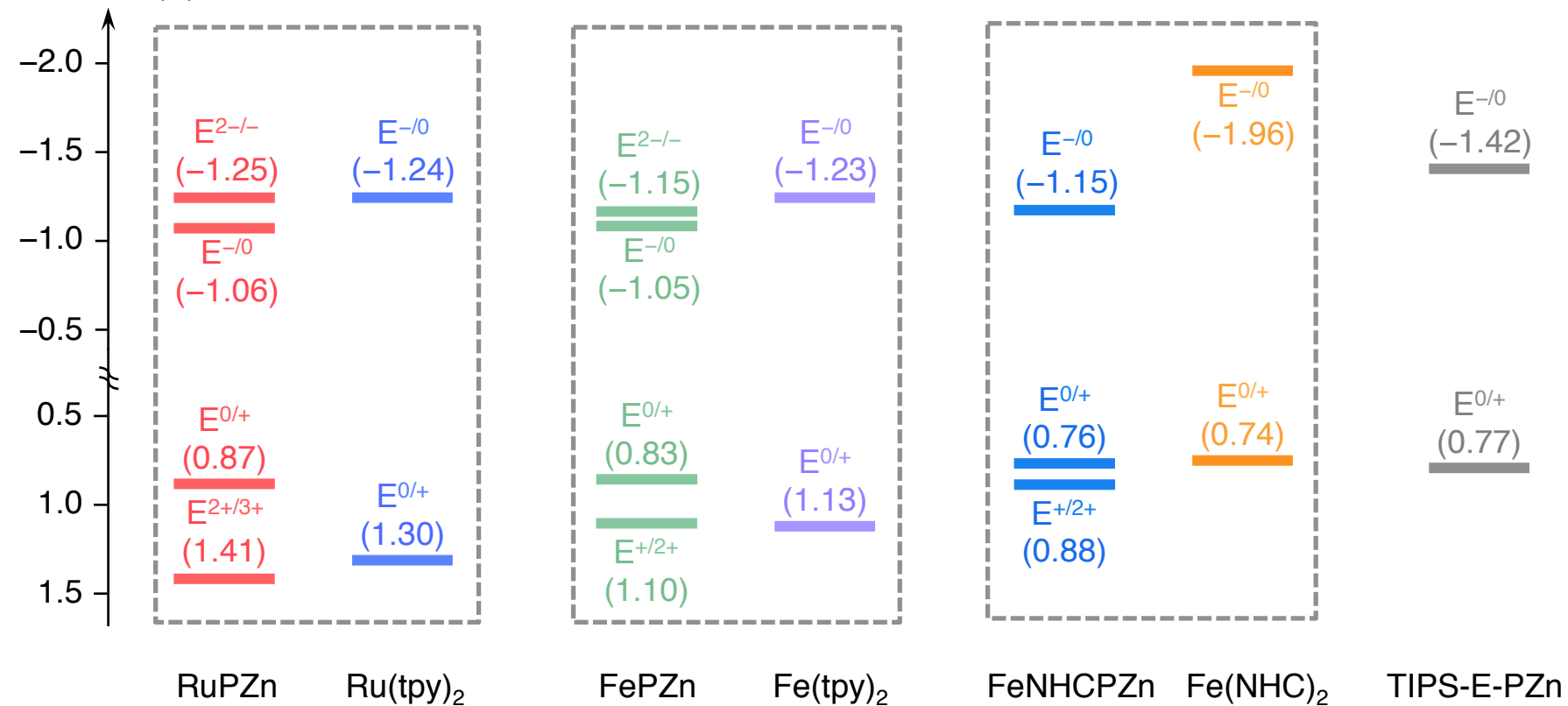
Figure 4. Jablonski diagrams illustrating the relative energetic arrangement of (**A**) FePZn and (**B**) FeNHCPZn selected electronic states and corresponding excited-state relaxation dynamics; (**C**) steady-state emission (λ_{ex} = 532 nm, P_{ex} = 1 mW) and (**D**) time-resolved emission (λ_{ex} = 405 nm) of FeNHCPZn in 1:1 MeCN:H$_2$O solvent at room temperature.
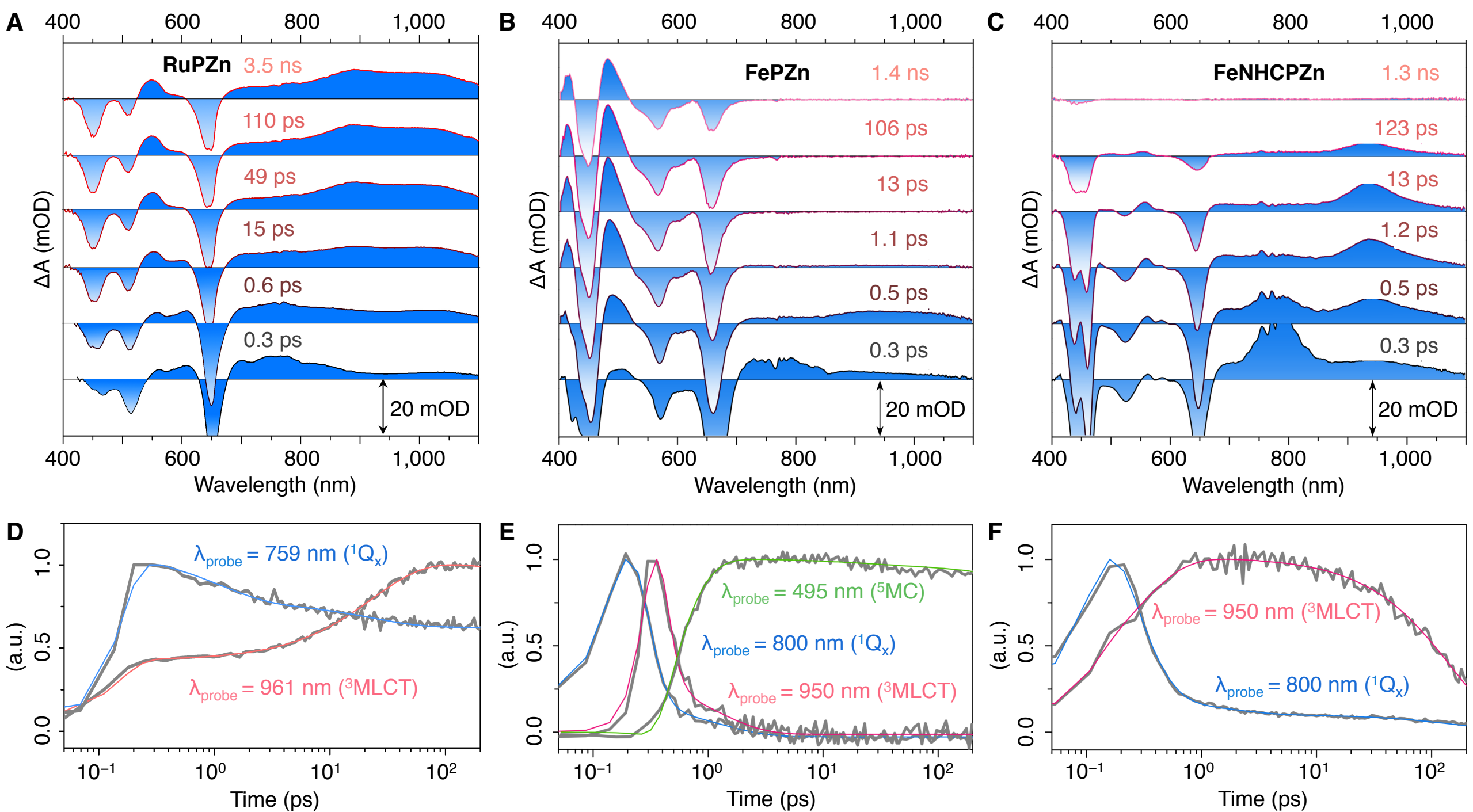
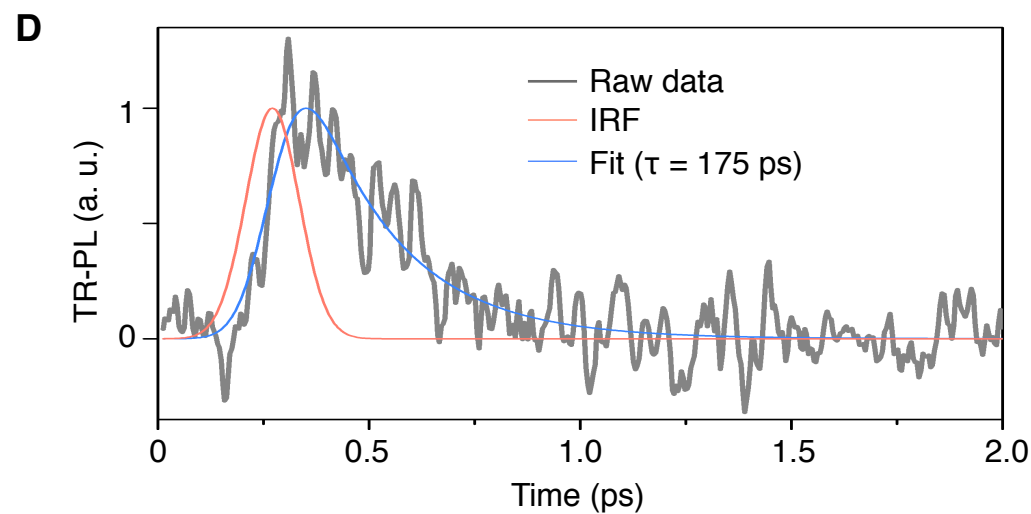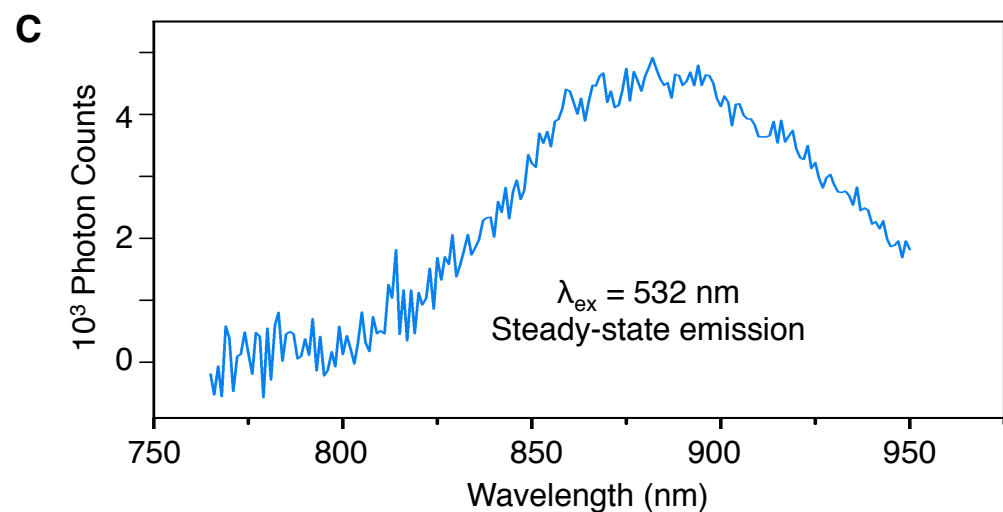**Figure 5.** B3LYP-computed singly occupied molecular orbitals (SOMOs) of the FeNHCPZn T$_1$ state.

RuPZn

FePZn

FeNHCPZn

$R = $

A RuPZn

- 3.5 ns
- 110 ps
- 49 ps
- 15 ps
- 0.6 ps
- 0.3 ps

20 mOD

ΔA (mOD)

Wavelength (nm)

B FePZn

- 1.4 ns
- 106 ps
- 13 ps
- 1.1 ps
- 0.5 ps
- 0.3 ps

20 mOD

ΔA (mOD)

Wavelength (nm)

C FeNHCPZn

- 1.3 ns
- 123 ps
- 13 ps
- 1.2 ps
- 0.5 ps
- 0.3 ps

20 mOD

ΔA (mOD)

Wavelength (nm)

D

$\lambda_{probe} = 759$ nm (^1Q_x)

$\lambda_{probe} = 961$ nm (^{3}MLCT)

(a.u.)

Time (ps)

E

$\lambda_{probe} = 495$ nm (^{5}MC)

$\lambda_{probe} = 800$ nm (^1Q_x)

$\lambda_{probe} = 950$ nm (^{3}MLCT)

(a.u.)

Time (ps)

F

$\lambda_{probe} = 950$ nm (^{3}MLCT)

$\lambda_{probe} = 800$ nm (^1Q_x)

(a.u.)

Time (ps)

A

S₁ — ~0.1 ps → ³MLCT

λ_Pump: 670 nm 1.85 eV

0.3 ps → ³MC, ⁵MC

S₀ — 5.4 ns

B

S₁ — 0.3 ps → ³MLCT, ³,⁵MC, E_MC

λ_Pump: 650 nm 1.91 eV

160 ps 1.53 eV

S₀

C

10³ Photon Counts vs Wavelength (nm)

λ_ex = 532 nm
Steady-state emission

D

TR-PL (a. u.) vs Time (ps)

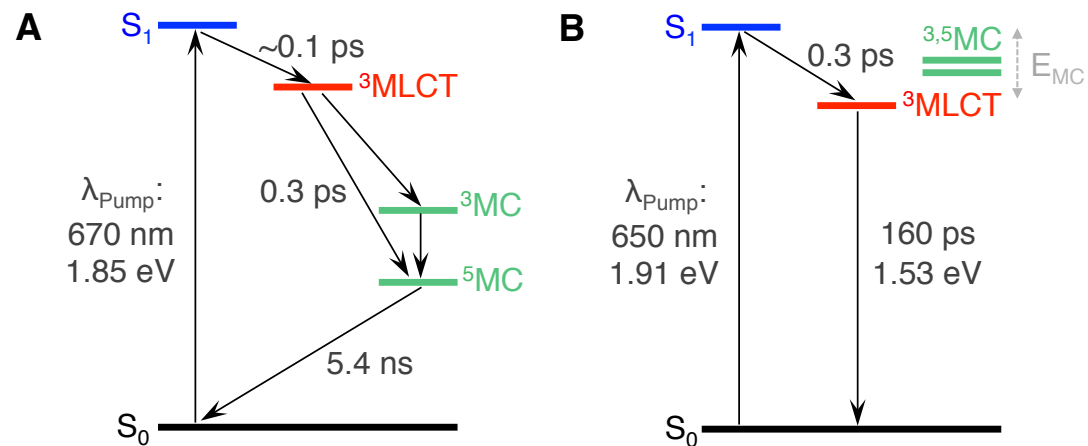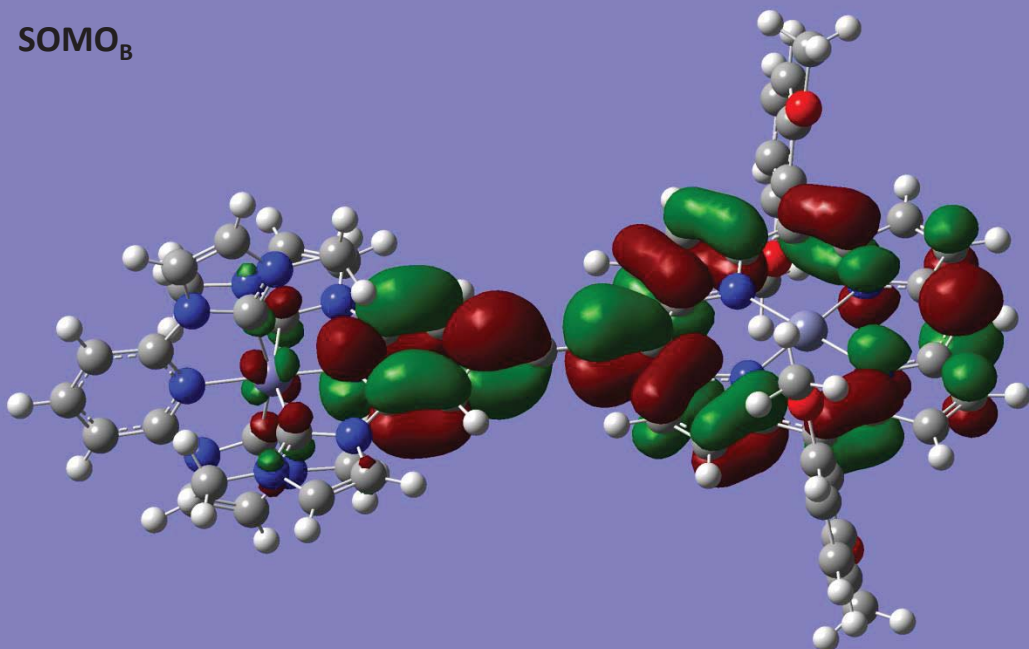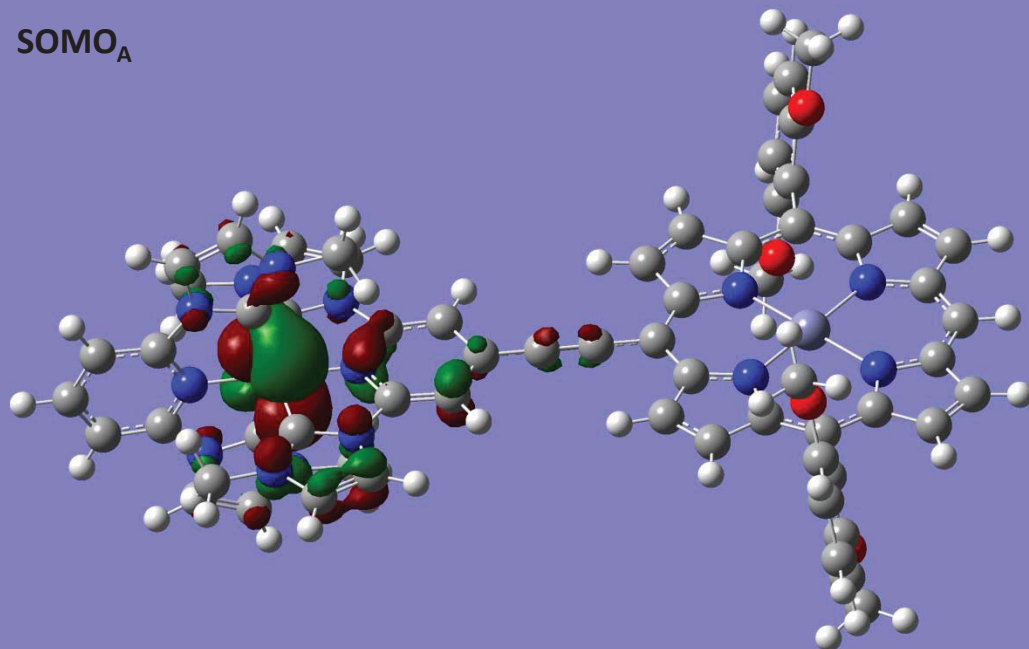— Raw data
— IRF
— Fit (τ = 175 ps)

SOMO_B

SOMO_A

Table 1. Ground-state singlet (S_0), and electronically excited triplet (T_1) and quintet (Q_1) state energetic minima (eV), computed using DFT and coupled cluster theory.[a]

	FePZn			FeNHCPZn			
	B3LYP	TPSSh	M06L	B3LYP	TPSSh	M06L	CCSD(T)
S_0	0.00	0.00	0.00	0.00	0.00	0.00	0.00
T_1	0.72	0.87	0.83	1.35	1.36	1.29	1.95
Q_1	0.23	0.43	0.50	3.05	3.04	2.75	3.70

[a] See Supporting Information.

Table 2. B3LYP-computed dipole moment components (X, Y, Z; Debye) of the ground and lowest energy triplet and quintet states for FePZn and FeNHCPZn; here the Fe–Zn axis is defined as the x-direction. The large dipole moment difference between the FeNHCPZn T_1 and S_0 states underscores the MLCT nature of its lowest energy electronically excited triplet state. Similar dipole moment magnitude changes between these FePZn and FeNHCPZn ground and excited states were obtained using TPSSh and M06L functionals.[a]

	FePZn			FeNHCPZn		
	X	Y	Z	X	Y	Z
S_0	58.33	−0.01	0.23	58.52	−0.02	0.13
T_1	58.40	0.00	0.14	88.11	0.14	0.21
Q_1	57.47	0.02	0.17	94.33	0.14	0.16

[a] See Supporting Information.